Atmospheric Research, 22 (1988) 149–181
Elsevier Science Publishers B.V., Amsterdam — Printed in The Netherlands

Development of a Continuous Flow Thermal Gradient Diffusion Chamber for Ice Nucleation Studies

DAVID C. ROGERS*[1]

Department of Atmospheric Science, University of Wyoming, Laramie, WY 82071 (U.S.A.)

(Received November 26, 1986; accepted after revision February 15, 1988)

ABSTRACT

Rogers, D.C., 1988. Development of a continuous flow thermal gradient diffusion chamber for ice nucleation studies. Atmos. Res., 22: 149–181.

A supercooled continuous flow, thermal gradient diffusion chamber has been developed to study the ice nucleating properties of natural or artificial aerosols. The chamber has concentric cylinder geometry with the cylinder axis alignment and airflow vertically downward. Sample airflow is 1 l min^{-1} and occupies the central 10% of the annular lamina; it is separated from the ice-covered walls by filtered sheath air. The wall temperatures are independently controlled over the range from about $-4\,^{\circ}C$ to $-25\,^{\circ}C$, so that the vapor concentration at the location of the sample lamina can be set to a well defined value between ice saturation and a few percent water supersaturation. There is a range of temperature and supersaturation values across the sample region; for lamina center conditions of $-15\,^{\circ}C$ and +1% with respect to water, the range is -14.6 to $-15.4\,^{\circ}C$ and +0.53 to +1.31%. Errors in temperature control produce variations estimated as $\pm 0.1\,^{\circ}C$ and ±0.23%. Typical sample residence time is about 10 s. Ice crystals which form on active nuclei are detected optically at the outlet end of the chamber. To enhance the size difference between ice crystals and cloud droplets, the downstream 25% of the warm ice wall is covered with a thermally insulating vapor barrier which reduces the vapor concentration to ice saturation at the cold wall temperature, so cloud droplets evaporate.

A mathematical model was developed to describe the temperature and vapor fields and to calculate the growth, evaporation, and sedimentation of water and ice particles. At 1% water supersaturation, the model predicts that ice particles will grow to about 5 μm diameter, and cloud droplets will achieve about 1 μm before they reach the evaporation section of the chamber. A different model was developed to describe the steady state airflow profile and location of the sample lamina.

Experimental tests of the chamber were performed to characterize the airflow, to assess the ability of the technique to detect silver iodide ice nucleating aerosols and to distinguish ice crystals from water droplets.

*[1]Present address: Department of Atmospheric Science, Colorado State University, Fort Collins, CO 80523 (U.S.A.)

0169-8095/88/$03.50

INTRODUCTION

It has been a common observation that concentrations of ice crystals in moderately supercooled clouds are substantially larger than those of ice nuclei measured under identical temperature and humidity conditions (Hobbs, 1975; Cooper and Saunders, 1980). As summarized by Mossop (1985), discrepancies between ice nuclei and ice crystal concentrations as large as four orders of magnitude are not uncommon. Possible explanations for the discrepancies include ice multiplication phenomena and inappropriate nuclei measurements. For many cases, cloud parcel histories must be closely examined to see if agreement should be expected at all. For example, in aircraft studies of orographic clouds, Cooper and Vali (1981) found that most ice crystals formed near the inflow region where supercooled water cloud first condensed, suggesting that ice crystals were forming by condensation-freezing or contact-freezing by very small aerosols.

Four different modes of heterogeneous ice nucleation are usually distinguished (Vali, 1985): *deposition, contact-freezing, immersion-freezing* and *condensation-freezing*. Since ice nuclei have some activity in varying degrees in each of these modes, the response of ice nuclei in an ice nucleus counter depends strongly on the nucleation modes that the instrument can activate. In this respect the continuous flow diffusion chamber design (e.g., Hussain and Saunders, 1984; Tomlinson and Fukuta, 1985) has several advantages over other current techniques for detecting ice nuclei.

(1) Ice and water nucleating aerosols are sampled in normal atmospheric concentrations.

(2) Aerosol samples are not supported on a substrate, as in the membrane filter technique (e.g., Gagin and Arroyo, 1969; Huffman, 1973; Zamurs et al., 1977).

(3) Large values of vapor supersaturation are possible and can be calculated and controlled with a high degree of accuracy. This is in contrast to mixing chambers (e.g., Langer, 1973) where the air sample is injected as a warm, moist, CCN-enriched turbulent jet into a cooled volume; temperatures and supersaturations are bounded, but the thermodynamic path of sample air is uncontrolled and unpredictable.

(4) The sample airflow is laminar, so particle trajectories are well defined; time resolution of the order of 1 s is possible.

This paper describes a cloud chamber that was designed and constructed to detect condensation freezing ice nuclei. The chamber has concentric cylinder geometry, which offers some advantages over flat parallel plate geometry: there are no "wall effects", the chamber is easily constructed, the inside of the chamber can be easily and rapidly accessed, and the chamber is less susceptible to air leak problems when operated below room pressure. The primary disadvantage of continuous flow diffusion chambers is that particle residence time is

limited to about 10 s or less in the supersaturated part of the chamber. Ice nuclei requiring exposure times in excess of this amount will not be detected. Continuous flow diffusion chambers should be capable of measuring ice nucleus activities by deposition and condensation-freezing modes if nucleation occurs within 1 or 2 s of the peak supersaturation. Because of the time requirement for aerosol collection by cloud droplets, it is unlikely that this technique is sensitive to contact-freezing nucleation.

The research described in this paper is an attempt to extend the technology of measuring ice nuclei. In the next section, a new design for a continuous flow thermal gradient diffusion chamber is presented. Following that, a mathematical description is given, and the results of some laboratory characterizations are shown. Measurements of natural ice nuclei with this chamber are being published separately.

DESCRIPTION OF CONTINUOUS FLOW CHAMBER

Design principles

The continuous flow chamber (CFC) described here uses a temperature gradient to produce vapor supersaturation in the region between two ice-covered walls. It was designed to operate between $-7°$ and $-20°$C and from ice saturation to water supersaturation. The chamber has concentric cylinder geometry with the cylinder axis vertical and airflow downward. Similar ice nuclei sampling chambers have recently been constructed by Hussain and Saunders (1984) and Tomlinson and Fukuta (1985), but their chambers were flat, with horizontal walls and horizontal airflow. These are similar to continuous flow parallel plate cloud chambers used to measure CCN at room temperatures, such as described by Hudson and Squires (1976). The concentric cylinder geometry has also been used for CCN measurements (Saxena and Carstens, 1971). Fig. 1a indicates the fundamental principles of operation: in the region between two ice-covered plates which are maintained at two different temperatures, linear steady state vapor pressure and temperature fields develop (heavy solid lines); but the saturation vapor pressures of water and ice are exponential functions, and consequently ice supersaturation is produced everywhere between the plates. If the temperature difference between the plates is large enough, water saturation may be exceeded, as for the case shown, where the warm plate is at $-4°$C and the cold plate is at $-16°$C. Notice that the maximum water and ice supersaturations are not at the same location.

Calculated chamber flow velocity profiles are shown in Fig. 1b. The aerosol sample is injected midway between the plates, with equal amounts of filtered sheath air on either side so that the sample temperature and vapor environment is relatively narrow and well defined. In horizontal diffusion chambers (warm plate on top), the aerosol lamina remains centered, but for vertical

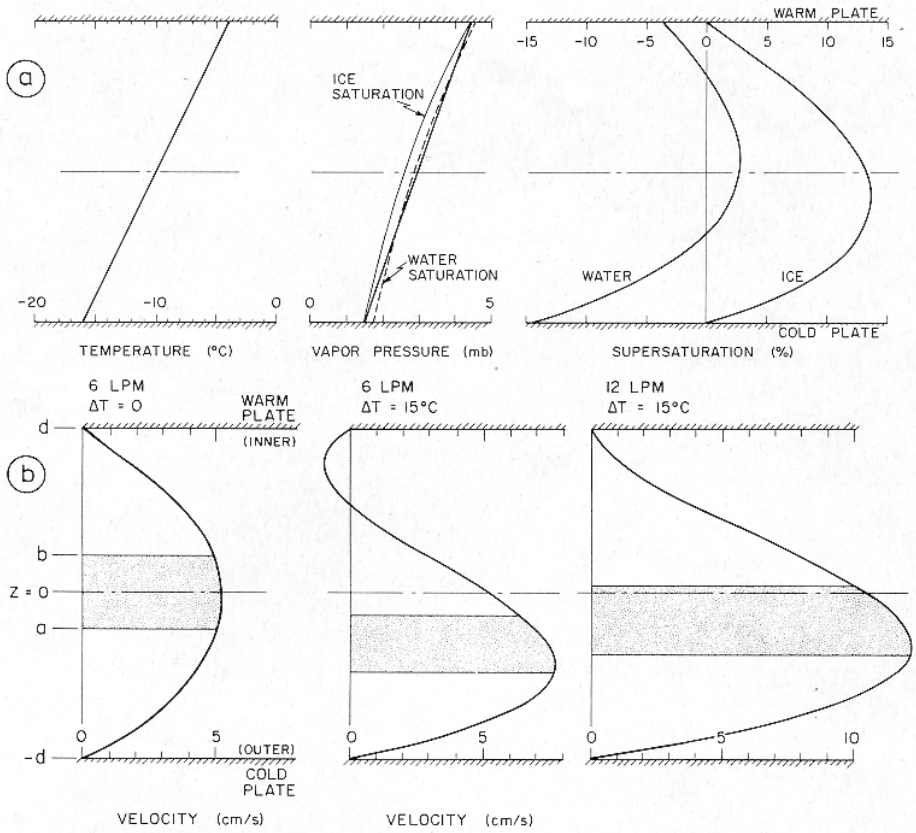

Fig. 1. Steady state profiles in a vertical continuous flow thermal gradient diffusion chamber having ice covered warm and cold plates. In b, velocity profiles are for no temperature difference ΔT between the plates (left) and for ΔT of 15 °C with two different total volume flows (center and right). Stippling shows lamina carrying aerosol sample which is 1/3 of the total volume flow. Gravity points right.

chambers a buoyant circulation is produced because of the temperature (density) gradient and gravity. This results in a skewed velocity profile and displacement of the aerosol lamina toward the cold side. As they are carried through the supercooled, supersaturated region, CCN and ice nuclei activate and grow large enough to be sized and counted at the outlet of the chamber.

In the present design, the concentric cylinders have radii 4.0 and 5.0 cm. Overall length of the cylinders is 46 cm. Typical operating ranges for the chamber are: sample temperature of $-10°$ to $-20°$C; temperature difference between the two plates of 0° to 20°C; supersaturation with respect to water (SS_w) -10 to $+10$%; supersaturation with respect to ice (SS_i) 0 to 30%; total flow 4 to 10 l min^{-1}; and particle residence time 5 to 10 s.

As shown in Fig. 1a, values of SS_w are small (+1.6%) in comparison with SS_i (+13.4%), so the diffusion growth of water droplets is expected to be much slower than ice crystals. If nucleation times are equivalent, then droplets and crystals should be distinguishable by size alone. Another feature in the chamber further enhances the size difference by evaporating the water droplets before they leave the chamber: the last 10 cm of the warm ice plate are covered with a thermally insulating vapor barrier, which allows the vapor and temperature fields to relax to conditions of the cold ice plate (colder temperature and large water subsaturation). An optical particle counter at the CFC outlet is used to detect particles.

Hardware and operating procedures

A schematic of the continuous flow chamber system is shown in Fig. 2. Aerosol and sheath air follow separate paths to the chamber where they are combined in a laminar fashion at the inlet manifold. At the chamber exit, all flow passes through the optical particle counter (OPC, Climet Model A6064A). The flow is controlled by a needle valve on the vacuum source. Flow rates of the total, aerosol and sheath air are measured by the calibrated pressure drop across the sheath air filter. Ice crystals produce voltage pulses in the OPC which are sized and counted by the multichannel analyzer (Nucleus Model 1024D).

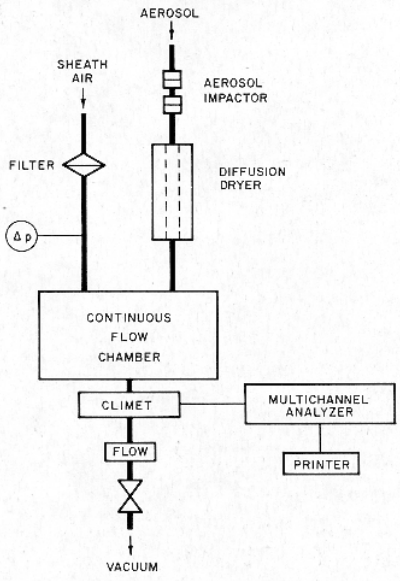

Fig. 2. Schematic of instrumentation and airflow (heavy lines) for measuring ice nuclei. ΔP is differential pressure gage. Climet is optical particle counter.

Photographs of the inner cylinder and sample injection region are shown in Figs. 3 and 4. Interior construction of the chamber is shown in Fig. 5. To ensure good thermal conduction, the chamber was constructed of copper and brass with joints silver-soldered. On the outer cylinder, the fluid from one temperature-controlled bath circulator is pumped at 30 l min^{-1} through 3/8 inch soft copper tubing, which is spiral-wound around the cylinder and lead–tin soldered for good thermal contact. The inner cylinder is a 2-l reservoir through which fluid from the other, independently controlled circulator is continuously pumped. The bottom 10 cm and the bottom cone of the inner cylinder are covered with 0.25 cm thick, closed cell plastic foam insulation. Thermal conductivity of this insulation was experimentally measured to be approximately a factor 850 smaller than that of copper or 5.3 smaller than that of ice. The diffusivity of water vapor through this insulation was experimentally estimated at 20 °C as a factor 400 smaller than through air. Rigid foam insulation, 5 cm thick, encloses the outer cylinder, and the whole is encased in 8-inch PVC pipe.

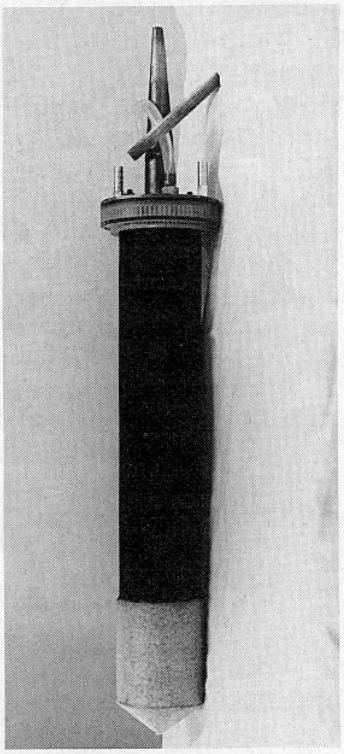

Fig. 3. Inner cylinder of CFC. During operation, relative airflow is from inlet manifold (top) toward insulated end (bottom).

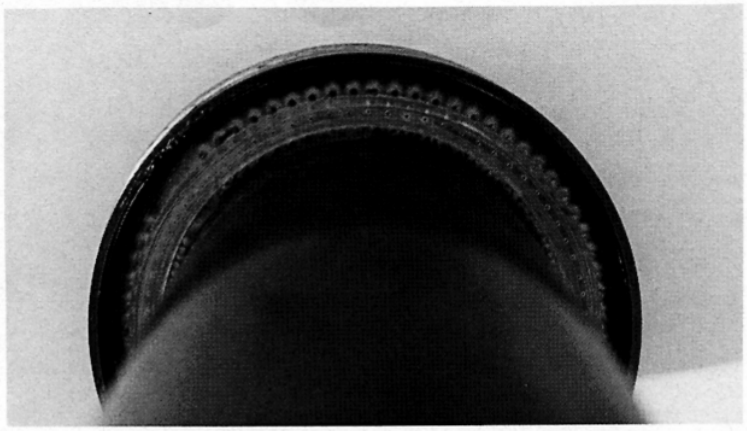

Fig. 4. End-on view of inlet manifold. Aerosol sample is injected through small holes between two rows of sheath air holes.

The chamber wall copper surfaces were ebonized to make them wettable. Attempts to use a fabric wicking material were not successful. The routine procedure for applying ice to the cylinder walls is to first cool the chamber to about $-5\,^{\circ}$C and then spray distilled water onto the cold metal. The slow freezing rate at $-5\,^{\circ}$C allows the water to spread somewhat and unite with other ice as it freezes. The ice on the walls builds up with successive applications to about 0.5 mm thickness with a smooth finish. After several hours of operation, frost grows on the cold wall at a rate depending on the temperature settings and ambient frost point. If the frost crystals grow longer than about 0.5 mm, they can be scraped off, and the ice surface smoothed by a warm hand.

In order to confirm the presence of supercooled water drops, an inspection window was constructed just upstream of the evaporation section of the CFC, where cloud droplets should be maximum size. Over the temperature range $-10\,^{\circ}$ to $-20\,^{\circ}$C, frequent inspections through this window with a microscope showed that no cloud particles were visible in a laser beam when the calculated $SS_w < 0\%$; cloud drops were always visible whenever SS_w was $+1\%$ or more; cloud visual density increased with SS_w; and with particle-free air, no cloud formed for any values of supersaturation.

Inner and outer wall temperatures were independently controlled by bath circulators of 600 W heating and cooling capacity (Forma Model 2325) and temperature control sensitivity of $\pm 0.02\,^{\circ}$C. The circulating fluid was antifreeze (ethylene glycol) and water in equal proportions. The assumption was made that the temperatures of the ice surfaces and copper walls were equal. The basis of this assumption is that the thermal conductivities of copper and ice are much larger than that of air: they are in the ratios 17000:93:1 for copper, ice and air, respectively. Several temperature measurements were rou-

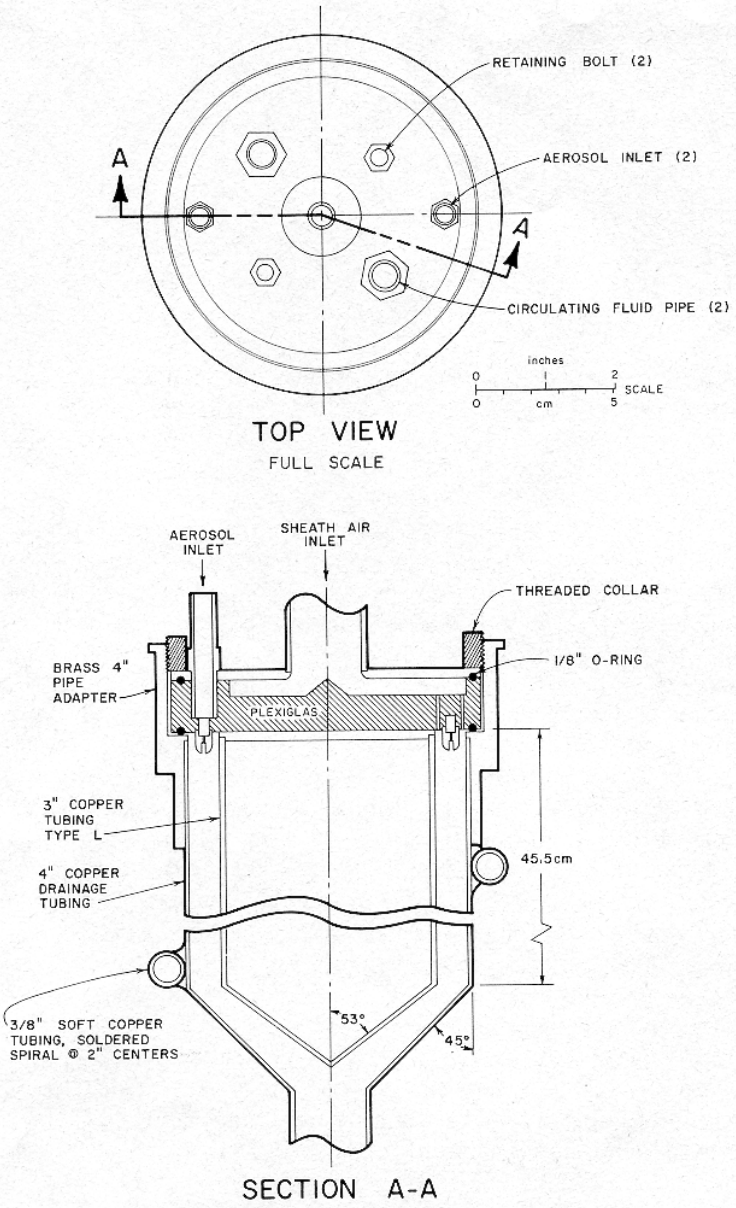

Fig. 5. Details of chamber construction.

tinely made: the circulator thermistor readout and control (digital, to 0.1°C); mercury-in-glass thermometers which were immersed in the bath (0.2°C divisions); copper-constantan thermocouples which were electrically insulated from, but in close thermal contact with the copper pipes carrying fluid from the CFC (sensitivity ±0.025°C per μV); and platinum resistance thermometers which measured the circulating fluid temperatures at the exit of the cold cylinder and at the entrance of the warm cylinder (accuracy of 0.05°C). Temperature readings from these various sources were consistent to within 0.3°C.

To assess the range of temperature variation along the cylinder wall, temperature differences were measured between the cooling fluid inlet and outlet pipes. Values of about 0.2°C were typical on both the cold and warm cylinders; e.g., fluid entered the warm cylinder at −6.8°C and left at −7.0°C, while at the cold cylinder, fluid entered at −19.9°C and left at −19.7°C. Since the temperature difference ΔT between the two cylinders is the fundamental quantity in determining supersaturation, a range of values can be deduced, 12.7°C to 13.1°C. For this instrument, the bath circulator thermistors were used for absolute temperature and the thermocouples in the CFC walls were used for temperature difference. With the temperatures set to give SS_w of +1% at −15°C at the aerosol lamina, an error of 0.1°C in ΔT produces an error of 0.23% in SS_w. During routine operation, values of ΔT were quite steady during the usual 10-min sampling periods; typical variations were about 0.1°C.

MATHEMATICAL MODELS

Two mathematical models of the environment inside the CFC were constructed to assist with the design and data evaluation. Both models assume that the chamber geometry is adequately represented with flat, parallel plates. The first model calculates the time-dependent evolution of the temperature and humidity fields and the growth and fallout of water and ice particles in slug flow. The second model calculates only the velocity profile for flow dominated by viscous and buoyant forces. More exact and complete mathematical calculations of the processes would require substantial additional effort but would not be much more informative for the present purposes. The difference in steady state temperature or vapor pressure fields for concentric cylinders versus flat parallel plates is at most 2% for the CFC dimensions. Furthermore, there remain significant fundamental questions about some of the physical processes (such as ice nucleation) which preclude a complete description.

Thermal and vapor diffusion fields

The mathematical problem and solution are the classical ones of heat and water vapor flux across a static air gap. Initially, the warm wall, the cold wall and the air are at three different temperatures. The solution form has been

given by Saxena et al. (1970) for the case of water-covered walls; the present solution is for ice-covered walls.

For the slug flow approximation, time and distance along the direction of flow are linearly related and are independent of distance from the wall. The Reynolds number is about 50, and the actual flow is viscous (Poiseuille). The actual velocity profile is nearly parabolic between the concentric cylinders since the wall separation is small compared with the radius of the cylinders (Knudsen and Katz, 1958). In comparison with the slug flow assumption, the Poiseuille velocity profile changes only the transient features of the humidity and temperature fields during the first few time constants (or about 2 s); thereafter, the steady state solutions of the temperature and vapor fields for slug and Poiseuille flow are identical. Because the temperature and vapor pressure gradients are larger, the fields develop faster in time for Poiseuille flow than for slug flow.

The one dimensional heat transfer equation is:

$$\frac{\partial T}{\partial t}=K\frac{\partial^2 T}{\partial X^2} \tag{1}$$

with boundary conditions:

$T(0,t)=T_c$

$T(a,t)=T_w$

$T(X,0)=f(X)=T_s$

where the temperature T is a function of both position X and time t; K is the thermal conductance of air (computed as a function of temperature and total pressure), $f(X)$ is the initial air temperature distribution (taken as constant), T_c and T_w are the cold and warm wall temperatures (located at X values of 0 and a), and T_s is the sample air temperature. The equation is solved by separation of variables and results in a Fourier series which converges rapidly:

$$T(X,t)=T_c+(T_w-T_c)\frac{X}{a} \tag{2}$$

$$+\sum_{n=1}^{\infty}\frac{2}{n\pi}[(T_s-T_c)+(T_w-T_s)(-1)^n]\sin\left(\frac{n\pi X}{a}\right)\exp\left[-\left(\frac{n\pi}{a}\right)^2 Kt\right]$$

The water vapor diffusion problem is similar to (1):

$$\frac{\partial e}{\partial t}=D\frac{\partial^2 e}{\partial X^2} \tag{3}$$

with boundary conditions:

$e(0,t)=e_i(T_c)$

$$e(a,t)=e_i(T_w)$$

$$e(X,0)=h(X)=e_l(T_d)$$

where e is water vapor pressure, D is the diffusivity of water vapor in air (computed as a function of temperature and total pressure), $h(X)$ is the initial vapor pressure distribution (constant), e_l and e_i are the saturation vapor pressures with respect to liquid water and ice, respectively, and T_d is the sample dewpoint. The model uses the Goff-Gratch equations for saturation vapor pressures (Goff, 1949).

The solution to eq. 3 is:

$$e(X,t)=e_i(T_c)+[e_i(T_w)-e_i(T_c)]\frac{X}{a}+\sum_{n=1}^{\infty}\frac{2}{n\pi}\{[e_l(T_d)-e_i(T_c)]$$

$$+[e_i(T_w)-e_l(T_d)](-1)^n\}\sin\left(\frac{n\pi X}{a}\right)\exp\left[-\left(\frac{n\pi}{a}\right)^2 Dt\right] \quad (4)$$

After a time interval τ the growth section ends and the droplet evaporation section begins. Boundary conditions change on the warm wall to be dry and insulated (i.e., zero heat and vapor fluxes). The steady state linear profiles of temperature and vapor pressure are achieved in the growth section. The thermal problem (1) has new boundary conditions. Define:

$$t'=t-\tau$$

$$T(0,t')=T_c$$

$$T(a,0)=T_w$$

$$\frac{\partial T}{\partial X}(a,\, t'>0)=0$$

$$T(X,\tau)=\text{linear profile}=(T_w-T_c)X/a$$

Again, the solution is a Fourier series:

$$T(X,t')=T_c+2(T_c-T_w)\sum_{n=1}^{\infty}\frac{(-1)^n\sin(Bx)\exp(-KB^2t')}{a^2B^2} \quad (5)$$

where $B=(2n-1)\pi/2a$.

Similar expressions are obtained for the vapor diffusion field with new boundary conditions:

$$e(0,t')=e_i(T_c)$$

$$e(a,0)=e_i(T_w)$$

$$\frac{\partial e}{\partial X}\,(a,t'>0)=0$$

$$e(X,\tau) = \text{linear profile} = [e_i(T_w) - e_i(T_c)]X/a$$

The solution is:

$$e(X,t') = e_i(T_c) + 2[e_i(T_c) - e_i(T_w)] \sum_{n=1}^{\infty} \frac{(-1)^n \sin(BX)\exp(-DB^2t')}{a^2B^2} \quad (6)$$

Values for τ are deduced from the length of the chamber ahead of the evaporation section and the average velocity in the sample lamina. The velocity is specific to volume flow and temperature settings, as explained on p. 166. The thermal and vapor fields are calculated using eqs. 2, 4, 5 and 6 for any location between the plates and at any time after an air sample is placed between the plates.

Particle growth and evaporation

Thus far in the model description, the only sinks or sources of heat or vapor are the ice-covered walls and the sample air. In this section, water and ice particles are added to the mathematical description. The additional equations compute water and ice particle growth and fallout due to gravity. Water and ice particles are assumed to nucleate and begin growing as soon as water and ice supersaturation, respectively, are exceeded. Both kinds of particles are assumed to be spherical; Kumai (1982) observed that 80% of incipient ice crystals formed by propane seeding were spheres (0.3–6 μm diameter). Crystals do not grow large enough in the chamber to justify including shape factors. The assumption is made that all growth is governed by a spherically symmetric diffusion field and by surface kinetic effects. Vapor pressure depression from dissolved substances and vapor pressure elevation due to surface curvature of very small particles are ignored for both water and ice particles. The growth of small ice particles is modeled analogous to droplets. The diffusion growth is given by the integrated form of Maxwell's equation (e.g., Fukuta and Walter, 1970):

$$d^2 = d_0{}^2 + F(T,d)\, SS\, \Delta t \quad (7)$$

where:

$$F(T,d) = \frac{8}{\dfrac{L_v^2}{kR_vT^2f_{3\alpha}} + \dfrac{R_vT}{e_{i,l}Df_{3\beta}}}$$

d is particle diameter, d_0 is initial diameter, SS is supersaturation (ice or water), Δt is time interval, L_v is latent heat of vaporization (ice or water), k is thermal conductivity of air, R_v is water vapor gas constant, $e_{i,l}$ is saturation vapor pressure (ice or liquid water, as appropriate) at temperature T, and the factors $f_{3\alpha}$

and $f_{3\beta}$ account for thermal accommodation and condensation (or deposition) surface kinetic effects (Fukuta and Walter, 1970) which can significantly retard the growth rates of small water and ice particles:

$$f_{3\alpha}=\frac{d}{d+\dfrac{2K\sqrt{2\pi M_\alpha RT}}{\alpha P(C_v+R/2)}} \tag{8}$$

$$f_{3\beta}=\frac{d}{d+\dfrac{2D}{\beta}\sqrt{\dfrac{2\pi}{R_v T}}} \tag{9}$$

where M_a is the molecular weight of air, R is the universal gas constant, α is the thermal accommodation coefficient, P is total atmospheric pressure, C_v is molar heat of air at constant volume, and β is the condensation (or deposition, γ) coefficient. Following common practice, α is taken as 1. There is a wide range of published values for β and γ, from <0.01 to 1 (e.g., Pruppacher and Klett, 1978; Mozurkewich, 1986). Some recent evidence from droplet growth studies suggests that β depends on whether the droplet is growing or evaporating (Hagen et al., 1986). Also, γ exhibits a temperature dependence, with values comparable to β near 0°C and increasing to near unity at about −50°C (Pruppacher and Klett, 1978; Fukuta, 1978). The present model uses 0.04 for both β and γ. Other values were also used to see if the choice made a significant difference in the simulations; the results are discussed later in this section.

Within each time step, total water mass is conserved so that water vapor is subtracted from the diffusion field when particles are growing, and conversely:

$$\text{vapor density}+\text{bulk water content}=\text{constant} \tag{10}$$

Using unprimed values to indicate the predictions of eq. 7 in a constant supersaturation field and primed values to indicate adjustment to include mass conservation, eq. 10 can be written:

$$\rho_v+W=\rho_v'+W'$$

or:

$$\frac{6(e-e')}{N\pi R_v T\rho}+d^3-d'^3=0$$

where ρ_v is vapor density, ρ is particle density, W is water concentration, and N is particle concentration. Substituting for d' from eq. 7:

$$\frac{6(e-e')}{N\pi R_v T\rho}+d^3-\left[d_0^2+F(T,d)\left(\frac{e}{e_{i,l}}-1\right)\Delta t\right]^{3/2}=0 \tag{11}$$

The equations describing particle growth (eq. 7) and water mass conserva-

tion (eq. 11) are solved iteratively within each time step using a Newton-Raphson method. The equations are coupled, with particle growth reducing supersaturation and particle evaporation increasing it. The conservation of heat energy could also be solved to account for heat sinks and sources in the sample volume (latent heat from growing and evaporating particles). For this chamber, the thermal and vapor fields are determined almost entirely by the walls; heat exchange from cloud particles is negligible by comparison. To simplify the mathematical model, the constraint of conservation of heat energy in air parcels in the chamber was not included. The temperature of droplets which may contain incipient ice nuclei is important for ice nucleation. Fukuta and Walter (1970) have shown that for typical SS_w of 1%, the temperatures of the environment and growing droplets differ by less than 0.1°C. Hence the temperature of particles is assumed to be the same as the chamber air at the same location.

Computations with identical initial conditions and successively higher concentrations N of water or ice particles showed no significant difference in the calculated size until the concentration exceeded ~ 3000 cm^{-3}, a value larger than anticipated during typical experiments with the chamber. This apparent insensitivity to N is because the conditions in the sample volume are dominated by the vapor and heat fluxes between the walls; particles in the sample volume make an insignificant difference unless they are large or occur in high concentration.

Cloud particles are assumed to be small spheres, and their fall speeds are described by the Stokes equation (Davies, 1966):

$$\text{Fall speed} = \frac{d^2 \rho g}{18 \mu} \tag{12}$$

where g is gravity, and μ is dynamic viscosity. Particle fall distances are accumulated during each time step for both ice and water.

In actual use, the model is given initial conditions of: warm and cold plate temperatures, temperature and dew point of the sample air, plate separation, concentration of particles (which become water droplets and ice crystals), orientation of the plates (horizontal or vertical, with respect to gravity), the location within the chamber where the calculation is performed (X, in the equations), and the time τ when the droplet evaporation section of the chamber begins. For horizontal orientation, the X-coordinate "falls" with the ice particles. The model uses 0.1 s time steps and runs for total time of 10 s, the maximum particle residence time in the chamber.

Some example model calculations are shown in Figs. 6, 7, and 8 for conditions of above or below water saturation and for vertical or horizontal orientation of the chamber. In these three figures, the steady state temperature in the center of the aerosol lamina is −15°C. Fig. 6 shows the evolution of a

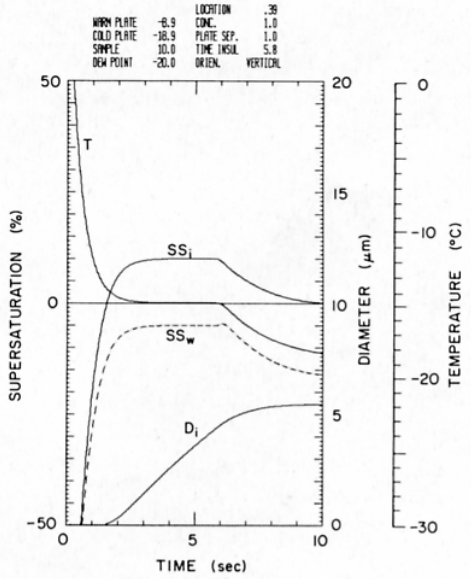

Fig. 6. Calculated temperature T and water and ice supersaturations (SS_w and SS_i) in CFC at the center of the aerosol lamina. D_i is diameter of ice crystal formed by deposition nucleation. Sampling temperature $-15\,^{\circ}C$. Boundary conditions (top) change on warm wall at 5.8 s.

sample at a location $X=0.39$ cm from the cold plate in the vertically oriented chamber; this value of X is the center of the lamina, as explained in the next section. The environment at this location is ice supersaturated after 1.5 s, and the temperature is within $0.5\,^{\circ}C$ of the steady state value after 1.9 s. Ice particles are assumed to nucleate by deposition as soon as $SS_i > 0\%$. They grow to 4.3 μm diameter at 5.8 s when the warm wall boundary conditions change; ice growth then ceases. Crystals ultimately reach 5.4 μm diameter.

Fig. 7 is similar to Fig. 6 except that the temperature difference between the plates is increased from $10.0\,^{\circ}C$ to $12.9\,^{\circ}C$, so water saturation is exceeded by 1% in this part of the chamber. The greater supersaturation results in larger ice particles and in the activation of water droplets. The droplets grow to about 0.3 μm diameter by 4.5 s and then evaporate afterwards in response to the altered boundary conditions. If a droplet contains a condensation freezing nucleus, it freezes as soon as $SS_w > 0\%$ and then grows rapidly in response to large SS_i, ultimately reaching about 6 μm. Crystals forming by deposition form earlier and are slightly larger, 7 μm. At the first time step when water saturation is exceeded, the environmental temperature is $-14.9\,^{\circ}C$, within $0.1\,^{\circ}C$ of the steady state value of $-15.0\,^{\circ}C$. Therefore, the steady state temperature is an appropriate estimate of the temperature of condensation freezing nucleation.

In order to assess the effects of β and γ on particle growth, some simulations

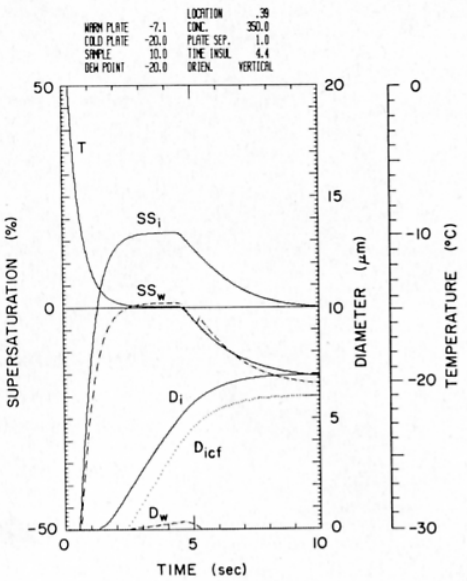

Fig. 7. Similar to Fig. 6, but larger temperature difference produces water supersaturation, and water droplets grow. Dashed line gives droplet diameter, D_w. Dotted line shows calculated diameter of ice crystal forming by condensation-freezing (D_{icf}). Boundary conditions change at 4.4 s, and droplets evaporate.

were done with values other than 0.04, namely 0.01, 0.1, 0.4, and 1. For sampling conditions of $-15\,^{\circ}C$ and $+1\%$ SS_w, small coefficients led to small particles and large coefficients gave large particles. Ice crystals were always larger than droplets by a factor 6 to 20 in diameter. The maximum sizes achieved by droplets ranged from 0.14 μm ($\beta=0.01$) to 2.0 μm ($\beta=1$). For ice crystals, the maximum sizes were, respectively, 2.8 μm to 12.3 μm. In all cases, when the boundary conditions changed, the droplets quickly evaporated to zero size, and the crystals stopped growing further.

Transient high supersaturations can occur in the sample injection region if the sample is both saturated and colder than the warm plate (Fitzgerald, 1970). No transient high supersaturations are expected with the CFC since the warm plate temperature never exceeds $-1\,^{\circ}C$ and the sample is brought nearly to room temperature ($20\,^{\circ}C$) in the inlet tubing and passes first through a diffusion dryer. No transient high supersaturations are predicted by the model for any of the typical operating conditions; a few simulations confirmed that the model will correctly predict transients when they are expected from appropriate initial conditions.

These simulations for a vertically oriented chamber are significantly different from those for a horizontal chamber because of the effects of gravity on the

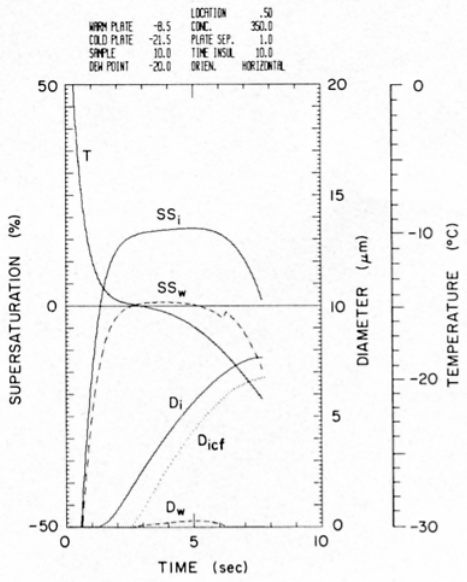

Fig. 8. Similar to Fig. 7, but chamber orientation and airflow are horizontal, so particles sediment from gravity. Values plotted are for a falling ice particle. The computation stops when the ice particle falls 0.5 cm and hits the lower wall.

particle motions. During the brief residence time in a horizontal chamber, activated and growing particles can sediment across the streamlines and may be deposited on the lower wall. The horizontal chamber of Tomlinson and Fukuta (1985) relies on this sedimentation to place small crystals on the bottom surface where they are later grown to visible sizes. Sedimentation can be significant: 5 to 10 μm diameter particles have terminal fall speeds of 0.1 to 0.3 cm s^{-1}, and they have to fall only 0.5 cm to hit the bottom (cold) surface. Fig. 8 shows sampling conditions similar to Fig. 7 ($-15°C$ and $+1\%$ SS_w), except that the walls and air flow are horizontal, and the boundary conditions do not change. The X-coordinate starts in the center of the chamber at 0.5 cm since there are no buoyant air circulations. The calculation follows a falling ice particle which hits the cold wall after 7.7 s, stopping the calculation. Other forces which cause particle drift (thermophoresis and diffusiophoresis) are neglected in the model since displacements of less than 0.1 cm are estimated for the case of greatest ΔT (15°C), according to the work of Sinnarwalla and Alofs (1973).

In addition to the numerical simulations for $-15°C$, calculations were done for $-10°C$ and $-20°C$ with β and γ of 0.04 and SS_w of -5%, -2%, -1%, $+1\%$, $+2\%$, and $+5\%$. They showed that the ultimate size achieved by ice crystals is consistently 5 to 10 μm diameter; crystals forming on deposition nuclei are 0.5 to 1.0 μm larger than those forming by condensation freezing.

With the exception of $+5\%$ SS_w, water droplets reach maximum diameters <1 μm and rapidly evaporate in response to the altered boundary conditions. For the $+5\%$ SS_w cases, the maximum is 2.8 μm, which also quickly evaporates.

Comparisons between this model and a model developed for NASA's Atmospheric Cloud Physics Laboratory (Nimitz and Plooster, 1980; Plooster, 1985) were made for the evolution of the temperature and humidity fields and the growth of water droplets. The NASA model has flat parallel plate geometry, parabolic velocity profile, continuous adjustment of water droplet size and concentration according to the CCN activation spectrum, and fixed boundary conditions. It does not simulate the growth of ice particles. Since it was designed to simulate cloud physics experiments in the Space Shuttle, it does not include the effects of gravity. Both models showed comparable growth rates of cloud droplets for $-15\,^{\circ}$C and SS_w of $+1\%$and $+5\%$. In the Nimitz and Plooster model, the temperature and humidity fields developed slightly faster (0.2 s) because larger gradients are present with parabolic flow; after about 3 s, the solutions were virtually identical.

Sample airflow

Because of the vertical plate orientation and the large temperature differences involved, a buoyancy-induced air circulation will be present; air near the cold plate will tend to sink, and air near the warm plate will rise. This circulation is added to the viscous Poiseuille flow and results in a rather skewed looking velocity profile, as shown in Fig. 1b for two values of temperature difference, 0° and $15\,^{\circ}$C, and for two different values of total flow, 6 and 12 l min^{-1}. Notice that some reverse flow is possible (negative velocity), and that the initially central aerosol sample lamina is displaced towards the cold side. The velocity profiles in this figure were calculated by approximating the annulus-temperature gradient flow as flat parallel plate-isothermal flow (parabolic velocity profile) and adding the buoyant velocity term (Sinnarwalla and Alofs, 1973):

$$V(Z,\Delta T)=\frac{3}{2}\bar{V}\left(1-\frac{Z^2}{d^2}\right)+\frac{\rho_a U g d^2 \Delta T}{12\mu}\left[\left(\frac{Z}{d}\right)^3-\frac{Z}{d}\right] \tag{13}$$

where V is the velocity, $\bar{V}$ is the mean velocity, Z is the distance from the centerline of the flow, $2d$ is the plate separation, ρ_a is the average air density and U is the volume coefficient of expansion of air. Equations for viscous annular and parallel plate flow from Knudsen and Katz (1958) were compared for the CFC geometry. Because the plate separation (1 cm) is much less than the radii of the cylinders (5 cm), the flat parallel plate approximation used here is not a critical compromise: for equal total flow, the velocity profiles differ by at most 2.5% over the central region carrying 95% of the flow.

In order that there should be no reverse flow, eq. 13 requires $\Delta T < 18\bar{V}T\mu/gd^2\rho_a$. Reverse flow can be avoided by increasing the total flow, so that the buoyancy circulation is small by comparison. Increased total flow results in smaller particle residence time in the chamber. In terms of affecting particle growth, the two effects are somewhat compensating: larger temperature differences produce larger buoyant velocities and larger supersaturations; thus smaller residence times are needed since the particles will be growing faster due to the larger supersaturations. However, because the sample lamina is displaced toward the cold wall, the processing conditions (temperature and supersaturation) for the aerosol sample are not those at the center of the chamber. The sample location depends on both total flow and temperature difference. The aerosol sample flow was adjusted to be a small fraction (1/10) of the total in order to reduce temperature and supersaturation differences across the sample lamina. The location of the lamina was calculated for a variety of $\bar{V}$, ΔT and sample flow fractions by integrating eq. 13 between the walls and the lamina coordinates such that half the mass flux is on either side of the sample lamina and solving the resulting fourth order polynomial equation for the roots (the lamina coordinates):

$$(1-q)\frac{Q}{2}=\frac{Q}{2d\bar{V}}\int_{-d}^{a} V(Z,\Delta T)\mathrm{d}Z=\frac{Q}{2d\bar{V}}\int_{b}^{d} V(Z,\Delta T)\mathrm{d}Z \tag{14}$$

where Q is the total volume flow rate, q is the fraction of total flow represented by the aerosol sample, and a and b are distances from the geometric centerline to the boundaries of the lamina (see Fig. 1b).

Fig. 9 shows calculated profiles of the velocity, SS_w, SS_i, and locations of the aerosol lamina for different operating conditions of Q, ΔT and T_α (aerosol lamina temperature) chosen for routine ice nucleus sampling work. The velocity was calculated from eq. 13, SS_w and SS_i from the steady state linear profiles of temperature and vapor pressure, and the aerosol lamina location from eq. 14. In these calculations, and in actual sampling with the chamber, total flow was adjusted to be 10% larger than the minimum needed to avoid reverse flow. Throughout the entire range of conditions shown, the aerosol lamina occupies the region extending from $X=0.36$ to 0.42 cm from the cold plate; thus the sample lamina center is at $X=0.39$ cm, which was used in the mathematical simulations discussed earlier. Fig. 9 also shows that the lamina is approximately centered on the SS_i profile but is offset from the peak of the SS_w profile. The variation of temperature and supersaturation across the lamina is not insignificant. For example, to achieve +1% SS_w at −15°C, ΔT of 12.9°C is needed between the warm and cold plates. Across the 0.06 cm width of the lamina, the temperature varies from −15.36° to −14.61°C, SS_i varies from 16.84 to 16.80%, and SS_w varies from +1.31% to +0.53%.

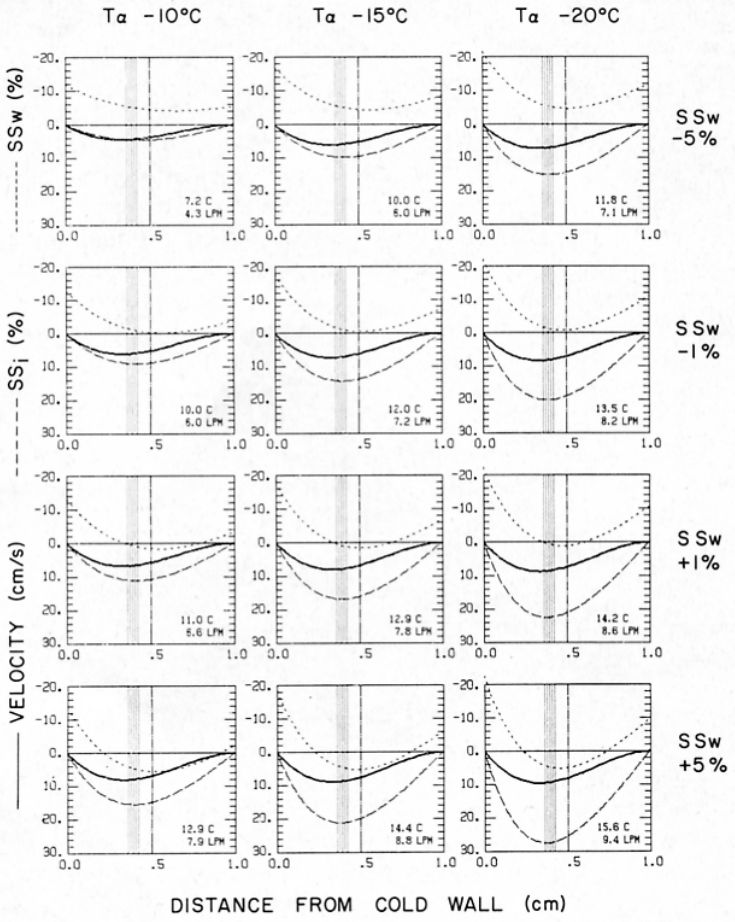

Fig. 9. Calculated profiles of vapor and flow velocity for routine sampling temperatures and water supersaturations. Each plot has warm wall on right and cold wall on left. Plots show supersaturations with respect to water SS_w (dotted) and ice SS_i (dashed) given in percent, airflow velocity (solid, cm s^{-1}) and calculated location of aerosol lamina (stippling) carrying 1/10 of total flow. Within each vertical column of plots, the central temperature of the aerosol lamina is constant T_α. Within each horizontal row of plots, SS_w in the center of the aerosol lamina is the same. Values of temperature difference between ice walls and total flow rate are shown in corners of each plot.

LABORATORY CHARACTERIZATIONS

Sample airflow

Some tests of airflow and aerosol residence time were performed using the CFC in series with the optical particle counter (OPC) and the multichannel

analyzer (MCA) in a dwell time mode. During these tests, the chamber walls were dry, and the wall temperatures were controlled. Pulses of aerosol-laden air were admitted into an otherwise steady stream of particle-free air. In dwell time mode, the MCA accumulates counts over a specified time increment in each channel (e.g., 0.1 s). An example aerosol pulse is shown in Fig. 10; there are no particles for the first 7.6 s, then there is a rather abrupt rise in concentration which persists for about 7 s, and the concentration then rapidly decays back to that of clean air. These time intervals were used to estimate the transit time and width of the aerosol pulse; the pulse width was defined as the time duration within which 90% of the counts occurred, and the transit time measured the lapse from when particles were first admitted to the inlet until 5% of the total was counted. In the case shown in Fig. 10, the pulse width at the inlet was 5.0 s and at the outlet 5.0 s; the transit time was 8.5 s.

Three factors influence the pulse transport characteristics of the CFC, and they are interrelated: the total flow, the temperature difference, and the fraction of total flow represented by aerosol. With Reynolds numbers of generally 30 to 100, flow through the CFC is expected to be laminar. Numerous experiments, such as Fig. 10, provided evidence of the laminar nature of the flow, including relatively smooth injection of the aerosol lamina. Fig. 11 shows the dependence of pulse width and transit time on aerosol fraction when total flow was fixed and the temperature difference was varied from 0° to 15°C. For all the cases shown, the pulse width at the inlet was 5.0 s. The figure demonstrates the expected trends: as the aerosol fraction increased, the pulse width increased (spreading due to the velocity profile) and the transit time decreased (with greater aerosol fraction, less time was needed to flush the tubing leading to the inlet with particle-laden air). Furthermore, as the temperature difference increased, the pulse width increased (greater velocity shear), and, for sufficiently large temperature differences, the pulse width increased drastically (reverse flow extended within the aerosol lamina). Significantly, two of the triangle data points in Fig. 11a show much larger pulse width, and the temperature difference for these points exceeded the reverse flow criterion of eq. 13.

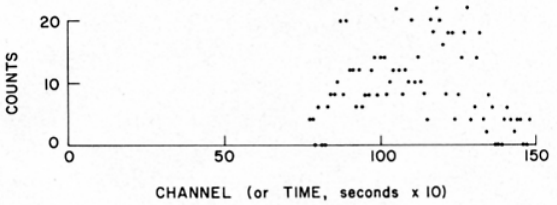

Fig. 10. Output from multichannel analyzer (MCA) showing passage of a pulse of aerosol at the outlet of CFC. Pulse duration was 5.0 s at inlet.

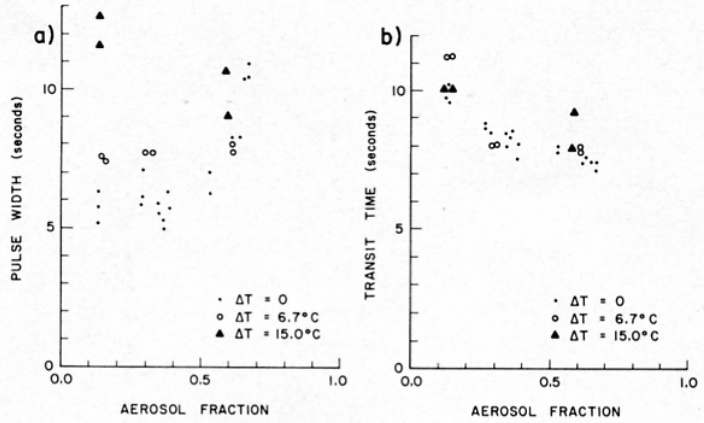

Fig. 11. Pulse width and transit times of 29 pulses of aerosol measured at outlet of the CFC for three temperature differences ΔT. All pulses were 5.0 s duration at inlet.

Optical particle counter

Fine resolution sizing and high efficiency of particle detection are required because particle size is used to distinguish ice particles from vestigial cloud droplets (haze). This requirement is met in the current instrument with the combination of the optical particle counter and the multichannel analyzer. All of the flow from the CFC passes through the OPC. The OPC inlet is 0.3 cm diameter and is located 10 cm below the end of the chamber outlet; they are connected by insulated tubing of 2.5 cm inside diameter. The MCA sorts voltage pulses from the OPC into one of 256 channels covering the size range 2 to 23 μm diameter, and it accumulates the data as a pulse height spectrum for the fixed duration of an experiment. The pulse height spectrum is translated into a size spectrum by a polynomial equation which was derived from calibrating the OPC-MCA system with monodisperse aerosols of known size, shape and refractive index. Monodisperse glycerin particles (transparent spheres of refractive index $n=1.47$), and particles of NH_4I ($n=1.70$) and NaCl ($n=1.54$) were produced with a Berglund-Liu vibrating orifice generator (Berglund and Liu, 1973; Thermo-Systems, Inc., Model 3050, St. Paul, Minnesota). Also, monodisperse latex particles (opaque white spheres, $n=1.58$) were produced by atomizing a hydrosol dispersion. Calibration aerosols were generated in diameters from 2 to 23 μm. For the glycerin particles, the voltage pulses were quite uniform, and the pulse height spectra were narrow (peak half-widths $<10\%$ of peak values). The accuracy of this system was estimated to be ± 0.7 μm. The resolution is size-dependent and amounts to 10% or less of the mean size above 6 μm diameter.

These estimates of accuracy and resolution apply to the glycerin aerosol

which was used for calibration – transparent spheres of homogeneous composition. Pulse height spectra for the salt particles invariably showed much wider distributions, probably due to the variations in shape, orientation and surface area of the aerosols. The salt particles had the appearance of cubes or clusters of cubes (NaCl) or of raisins (NH_4I). Perhaps the larger voltage pulses resulted from specular reflections off prism facets of optimally oriented salt particles. A similar broadening is expected for ice crystals if they have prism facets as well formed as the salt. Thus, in spite of the excellent accuracy and resolution capabilities of the system for transparent spheres, there is reduced capability for particles with faceted shapes. Crystals which form by condensation freezing probably begin as small spheres, but for deposition nucleation, the incipient crystal shape is unknown. In cold room propane seeding experiments, Kumai (1982) found 80% of the ice crystals younger than 0.5 s and 0.3 to 6 μm in size were spherical. At later times, the habits of crystals smaller than 100 μm were primarily hexagonal plates and columns. The time needed for small frozen drops to alter their shapes from spherical and begin showing facets and hexagonal symmetry is not known.

The ability of the Climet-MCA system to size water droplets is expected to be as good as for glycerin, and the calibration based on glycerin should be valid for water drops since the effect of refractive index is small for the Climet sensor (Cooke and Kerker, 1975). Thus the optical system performs very well as a particle size discriminator for the CFC in that small water droplets can be precisely sized, and larger ice crystals will be sized as large as or larger than their true sizes because of the broadening phenomenon. Coincidence errors in the Climet are not significant for the present application.

Inlet particle impactor

Natural concentrations of dry aerosol particles of 5 to 10 μm diameter are similar to the concentrations expected for natural ice nuclei at $-15\,^{\circ}C$, of the order 1 per liter. In order to avoid errors due to counting these large dry particles as ice crystals, an aerosol jet impactor was constructed for the sample inlet to remove particles larger than 5 μm diameter (Fig. 4). Calculations of collection efficiency for the design followed Ranz and Wong (1952). The effectiveness of the impactor was measured experimentally with the OPC. Two impactors were cascaded in series, with the outlet of one leading to the inlet of the next in order to increase the efficiency. Fig. 12 shows the calculated and measured efficiencies of particle removal versus particle size for three different typical flow rates. The measurements were obtained in a dust-laden environment with and without the impactors on the OPC inlet. Even for the lowest flow rates (poorest impaction efficiency), fewer than 7% of the particles larger than 6 μm passed through the two stage impactor.

In addition to this deliberate effort to control the size distribution of sample

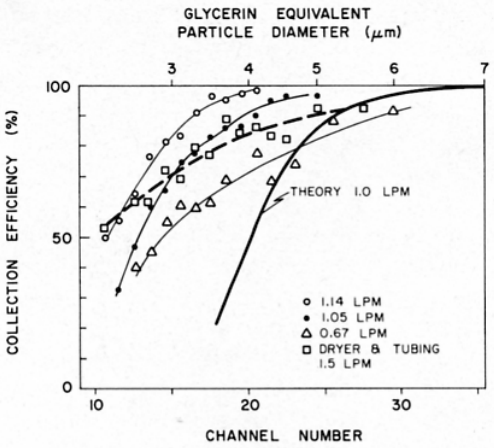

Fig. 12. Theoretical (Ranz and Wong, 1952) and measured impaction efficiencies of aerosol inlet impactor for three different flow rates. Also shown is particle removal efficiency of inlet tubing and diffusion dryer.

aerosols, the majority of large aerosols was lost to sedimentation and impaction within the inlet tubing and diffusion dryer. Another experiment with the OPC estimated this loss; the results are also shown in Fig. 12. Even with no impactors on the inlet, only about 8% of the particles larger than 5 μm were transported through the tubing and to the CFC. Overall, the particle transmission efficiencies are cumulative and multiplied. Overall, only 0.6% of the aerosols larger than 5 μm enter the CFC. For higher flow rates, this fraction is less than 0.1%. Therefore, the likelihood of erroneously interpreting large particles at the outlet of the CFC as ice crystals is substantially reduced, and essentially all particles larger than 5 μm grow to that size inside the chamber and can be interpreted as crystals which form on active ice nuclei.

The uncertainty arises that perhaps a significant number of ice nuclei are present in the sample air as large particles which are removed by the impactor and therefore are not sampled by the CFC. This problem is common to almost all ice nuclei sampling techniques, since particle losses in the tubing and inlet areas selectively, if unintentionally, remove large aerosols by impaction or sedimentation (with the possible exception of open face filter sampling).

Experiments with silver iodide aerosols

Some limited experiments with artificial ice nuclei were performed to assess the performance of this instrument. In particular, proof was sought that the fundamental assumptions about ice nucleation and growth in the CFC could be verified for a relatively well known ice nucleating aerosol, and that the ideas

and theoretical predictions of the evaporation of water droplets could be experimentally demonstrated.

The artificial nucleant used in these experiments was an atomized hydrosol of AgI-NH_4I complex (Vali et al., 1978). The hydrosol was prepared by adding a small amount of AgI-NH_4I complex solution to distilled water, whereupon AgI precipitated. Most of the AgI particles were a few tenths of a micrometer in size. When this hydrosol was atomized, the aerosol particles were not pure AgI, but had some residue of NH_4I. This added salt has several effects. It increases the ice nucleating activity over pure AgI. It is hygroscopic, so the AgI particles behave as wettable but insoluble CCN, and the aerosol was shown by Vali et al. to nucleate ice by both contact and deposition modes. Because of its high activity as both a CCN and an ice nucleus aerosol, it was expected to also nucleate ice via condensation-freezing.

The aerosol was generated in a Constant Output Atomizer (COA, Thermo-Systems, Inc., Model 3075) and then forced under pressure through a diffusion type dryer and through an electrostatic size classifier (Thermo-Systems, Inc., Model 3071) to extract a selected monodisperse fraction for study. This fraction was then electrically neutralized in a radioactive type aerosol neutralizer and stored in a 10-liter flexible bag of Velostat (an electrically conductive plastic material made by 3M Company). The CFC sampled from the bag for 1-min time periods and used about one liter of aerosol per sample run.

Results are given for two different aerosols, 0.06 μm and 0.09 μm diameter. Both aerosols were tested at $-15\,^{\circ}C$ over a range of vapor saturations. Pulse height spectra measured by the OPC-MCA system at the outlet of the CFC are shown in Figs. 13 and 14. Counts of zero particles per 10 channel bin were plotted as 0.1 on the logarithmic ordinate. The figures show that no particles larger than 5 μm were seen at the lowest supersaturations. As supersaturation increased, both the size and concentration of particles larger than 5 μm (ice crystals) increased.

An impactor similar to that used to remove large aerosols was used at the CFC outlet to impact ice crystals onto a glass slide for microscope examination. The slide had a thin layer of vacuum grease to hold the crystals. A microphotograph of a crystal impaction sample from one of the 0.09 μm AgI tests appears in Fig. 15. For this sample, the OPC was replaced with the crystal impactor; other experimental conditions were the same. The particles are approximately 6 μm in diameter but are not easily recognized as ice crystals. The images are similar to Kumai's (1982) in that only a few suggest hexagonal shapes. The size distribution of 98 crystals from this impactor sample is also plotted on Fig. 14. There is a significant difference in the actual sizes and that deduced from the OPC calibration data. The ice crystal pulse height spectrum is considerably broadened and indicates optically larger particles were present. Analogous to the NaCl calibration aerosol, this broadening and increase in apparent size may be due to the importance of crystal shape and orientation:

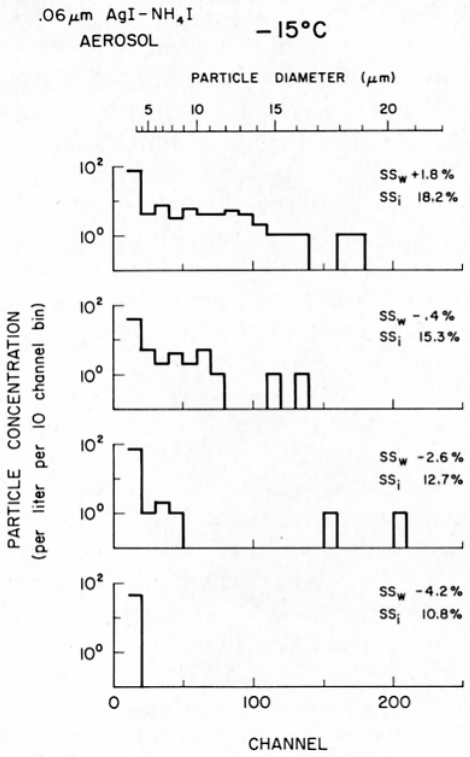

Fig. 13. Four pulse height spectra of crystals nucleating on 0.06 μm monodisperse AgI-NH_4I aerosol at $-15°C$ and four different values of water or ice supersaturation which increase in value from the bottom spectrum to the top spectrum. Particle diameter is based on calibration with monodisperse glycerin particles.

specular reflections from crystal facets may scatter as much light to the photomultiplier tube as much larger transparent spheres. The ice particle growth model predicted crystal diameters from 5.5 to 7.5 μm for all the tests shown. It appears that the OPC can be used to detect ice crystals in this size range, but impaction samples may be required if accurate information on crystal size is needed.

Fig. 16 shows a more conventional presentation of these AgI ice nucleus data, where the measured concentrations are plotted against supersaturation. The concentrations are based on the pulse height spectra and show the concentration of particles larger than channel 30 (6 μm diameter for a transparent sphere). This size was selected as appropriate for discriminating the smaller water or haze droplets from the much larger ice crystals. If the size had been chosen as 10 μm, similar results would have been obtained, but the concentrations would be reduced by approximately a factor 2. The values shown here for

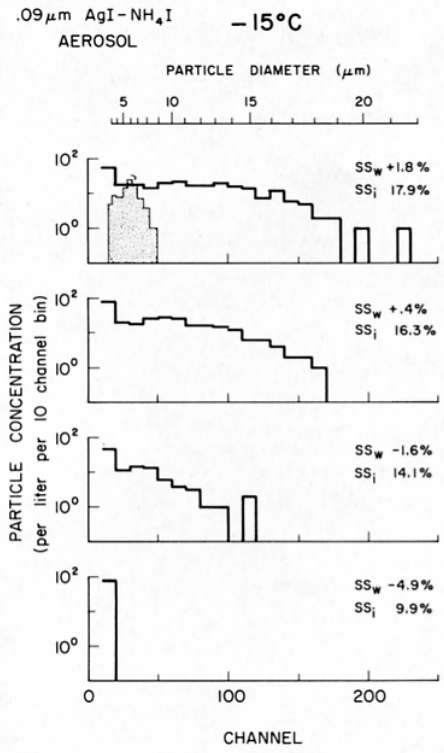

Fig. 14. Same as Fig. 13, but 0.09 μm aerosol. Also shown (stippled) on +1.8% SS_w graph is size distribution of 98 ice crystals from impactor sample, sized by microscope.

this aerosol are in approximate agreement with contact freezing measurements as given in Vali et al. (1978). The response of the aerosol to increasing supersaturation was quite strong and seemed to be rather like a threshold or step function which rises rapidly below water saturation and slowly at higher supersaturations. This kind of nucleating behavior was also observed in Tomlinson's (1980) experimental studies with thermally generated AgI.

These experiments with AgI demonstrated the ability of the CFC to activate and detect ice nuclei. The assumptions about ice nucleation and growth were shown to be reasonable for the particle growth model, but they are inadequate for completely characterizing the nucleating response of the AgI aerosol. The results suggest that deposition and condensation-freezing ice nucleation can be measured with this technique.

Experiments above freezing

There are several sources of uncertainty in identifying ice crystals at the outlet of the CFC on the basis of optical size alone. First, the sizes of ice crystals

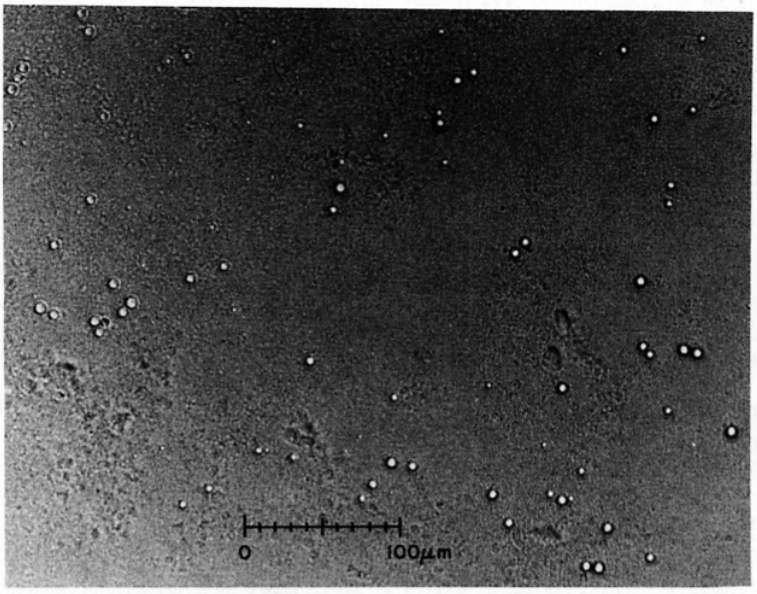

Fig. 15. Microphotograph of ice crystal impaction sample.

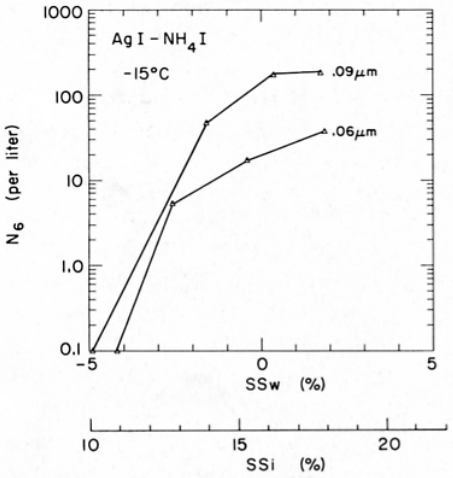

Fig. 16. Supersaturation dependence of ice nucleus concentrations for monodisperse AgI-NH_4I aerosol. Temperature was $-15\,^{\circ}C$ for all data points.

are difficult to predict because of unknown nucleation rates and uncertainties in growth rate at small sizes. Second, the evaporation of cloud droplets may not be complete before the sample enters the optical counter. In this section,

the feasibility of discriminating ice crystals from droplet residues is examined from several different perspectives.

The ideal case of a perfectly insulating and vapor impervious barrier on the warm wall of the droplet evaporation section is not physically realizable. Experimental estimates of the heat and vapor fluxes through the insulation suggested that the zero vapor flux assumption is better justified than the zero heat flux assumption. To evaluate these effects, the particle growth model was modified so that in the droplet evaporation section, the boundary conditions were zero vapor flux but the same wall temperature and heat flux as upstream of the insulation. This case represents a hypothetical condition much worse than is realized in the chamber. For $+5\%$ SS_w and $-15°$C upstream, the calculations showed that removing the warm vapor source caused negative water *and* ice supersaturations downstream. Water drops evaporated sooner, and ice particles also began to evaporate. Ice particles were still larger than 5 μm at the end of the evaporation section. Thus, the concept of using an evaporation section to enhance the difference in size between water and ice particles was reinforced even for this worst case approximation.

For conditions of $+1\%$ SS_w at $-10°$, $-15°$ and $-20°$C in the growth section, the residence times of droplets in the evaporation section were estimated from the airflow calculations to be about a factor 2 greater than what the growth model predicted was needed to evaporate the drops completely. However, for $+5\%$ SS_w the droplets grow larger, flow rates are greater, and the residence times are approximately a factor 2 less than needed. Thus, at $+5\%$ some small water droplets are expected to reach the outlet.

The problem of distinguishing crystals from droplets was also studied experimentally by operating the CFC at a warm temperature ($+15°$C) to provide information on the droplet background to be expected at cold temperatures. In order to retain water on the walls of the CFC, paper towels were used as wicking material; they were saturated with water and held in place by surface tension. Measurements of natural air were performed over the range 0% to nominal 9.8% SS_w.

The results are summarized in Fig. 17 as pulse height distributions showing the response of natural aerosol to successively higher SS_w. The bottom spectra show dry aerosol as sampled directly into the optical counter and also at the outlet of the dry CFC where the influence of the aerosol impactor and tubing and dryer losses is apparent. At 0% SS_w, a few haze drops appeared. From $+0.43\%$ to $+9.8\%$ SS_w, there were consistent increases in both total numbers and sizes of droplets, indicating nucleation and growth of water droplets. Note the distinct difference in the shape of the distribution in Fig. 17 (cloud droplets) compared with Figs. 13 and 14. Fig. 17 suggests that the size of the largest droplets can be used as a threshold to discriminate water droplets from ice crystals (e.g., channel 30 or 6 μm at SS_w of $+1\%$), such that all larger particles are considered to be crystals. These experiments at $+15°$C overestimate the

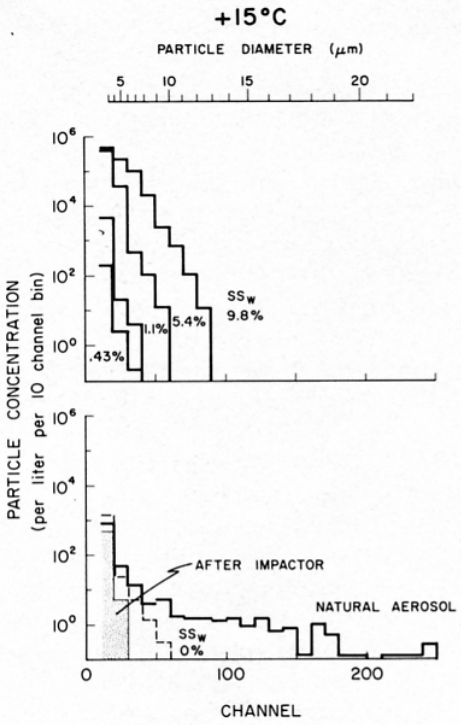

Fig. 17. Results of a series of warm temperature experiments shown as pulse height spectra of particles. Particles larger than about 5 μm were removed from natural aerosol by the impactor (bottom figure). The remainder went into the chamber where some particles grew as CCN. Compare with Figs. 13 and 14 which indicate large particles are only associated with active ice nuclei.

size that droplets would achieve at $-15\,^{\circ}$C for equivalent SS_w and growth time since the theoretical growth rate at $+15\,^{\circ}$C is about a factor 4 larger than at $-15\,^{\circ}$C because of thermal dependencies of saturation vapor pressure, latent heat, diffusivity and thermal conductivity. Thus, the sizes of residual droplets in the CFC at supercooled temperatures are overestimated by the tests at $+15\,^{\circ}$C. The evaporation section will further reduce droplet sizes below those observed at $+15\,^{\circ}$C.

CONCLUSIONS

A technique for measuring ice nuclei both below and above water saturation was developed using a continuous flow thermal gradient diffusion chamber. A mathematical model was constructed to simulate the development of thermal and vapor fields and the response of cloud active particles to these fields. The model calculations indicated that ice nuclei would produce crystals of 5 to 10

μm diameter in the chamber. Experimental tests confirmed the concepts of chamber operation, particle nucleation and growth, and optical detection. Within the sample lamina, the ranges of temperature and SS_w are typically less than 1°C and 1%. Errors in temperature control produce variations of about ± 0.1°C and ± 0.23%.

The advantages provided by this design could be applied to nucleation and growth problems that are otherwise intractable. Some ideas for future experimental studies with the CFC are offered here. The growth rate of small ice crystals could be studied by varying the total flow with supersaturation fixed. The measured change in particle size could be used to extrapolate to the nucleation point and compare with theoretical predictions. Nucleating behavior of different artificial ice nucleants could be studied for deposition and condensation freezing modes. Other experiments to separate the size of ice nuclei could be pursued. For example, in a manner similar to Twomey's (1972) studies of CCN size, natural aerosol could be first sorted by size, and the resulting ice nucleus activity could be related to aerosol size. Another study might use a continuous flow CCN chamber attached to the inlet of the CFC to grow active CCN at warm temperatures and separate them by impaction from the non-activated aerosol. Since CCN activity is probably a slowly changing function of temperature, the contribution of condensation-freezing ice nuclei could be deduced by comparing ice nucleus measurements for aerosol containing different fractions of the most active CCN. The fundamental parts of the chamber are small enough that the design could be adapted to mobile use. The temporal response capabilities would be well suited for aircraft-based studies. It is suggested that doubling the entire length of the chamber would improve the capabilities of this instrument. It would provide twice the crystal growth and droplet evaporation time and enhance the size differences.

ACKNOWLEDGEMENTS

Funding for this research was provided by several different sources: National Science Foundation Grant No. ATM-7717540, National Aeronautics and Space Administration Grant No. NAS8-33150, and the Department of Atmospheric Science, University of Wyoming. Preparation of the final manuscript was partially supported by NSF Grant No. ATM-8519370. The author is grateful to the faculty and staff of the University of Wyoming's Department of Atmospheric Science for their support, advice and encouragement. Patrick Kelly provided excellent machine work and technical advice. Professors Gabor Vali and Al Cooper contributed extensively to the instrument design and data interpretation. Susan Allen expertly drafted the figures.

REFERENCES

Berglund, R.N. and Liu, Y.H., 1973. Generation of monodisperse aerosol standards. Environ. Sci. Technol., 7: 147–153.

Cooke, D.D. and Kerker, M., 1975. Response calculations for light-scattering aerosol particle counters. Appl. Opt., 14: 734–739.

Cooper, W.A. and Saunders, C.P.R., 1980. Winter storms over the San Juan Mountains, Part I. Microphysical processes. J. Appl. Meteorol., 19: 927–941.

Cooper, W.A. and Vali, G., 1981. The origin of ice in mountain cap clouds. J. Atmos. Sci., 38: 1244–1259.

Davies, C.N., 1966. Deposition from moving aerosols. In: C.N. Davies (Editor), Aerosol Science. Academic Press, London, pp. 393–446.

Fitzgerald, J.W., 1970. Non-steady-state supersaturations in thermal diffusion chambers. J. Atmos. Sci., 27: 70–72.

Fukuta, N., 1978. Ice crystal growth kinetics and accommodation coefficients. Conference on Cloud Physics and Atmospheric Electricity, Issaquah, Wash., Am. Meteorol. Soc., Boston, pp. 103–108.

Fukuta, N. and Walter, L.A., 1970. Kinetics of hydrometeor growth from a vapor-spherical model. J. Atmos. Sci., 27: 1160–1172.

Gagin, A. and Aroyo, M., 1969. A thermal diffusion chamber for the measurement of ice nuclei concentrations. J. Rech. Atmos., 4: 115–132.

Goff, J.A., 1949. Final report of the working subcommittee of the International Joint Committee on Psychrometric Data. Trans. Am. Soc. Mech. Eng., 71: 903–913.

Hagen, D., Alcorn, M., Kassner, J., Carstens, J., Hopkins, R., Schmitt, J., Trueblood, M., Walker, W. and White, D., 1986. UMR cloud simulation studies of droplet growth: Investigation of condensation coefficient. Conference on Cloud Physics. Snowmass, Colo., Am. Meteorol. Soc., Boston, pp. c1–c4.

Hobbs, P.V., 1974. Ice Physics. Oxford University Press, Oxford, 837 pp.

Hobbs, P.V., 1975. The nature of winter clouds and precipitation in the Cascade Mountains and their modification by artificial seeding, Part I. Natural conditions. J. Appl. Meteorol., 14: 783–804.

Hudson, J.G. and Squires, P., 1976. An improved continuous flow diffusion cloud chamber. J. Appl. Meteorol., 15: 776–782.

Huffman, P., 1973. Supersaturation Dependence of Ice Nucleation by Deposition for Silver Iodide and Natural Aerosols. Ph.D. Dissertation, Department of Atmospheric Science, University of Wyoming, 124 pp.

Hussain, K. and Saunders, C.P.R., 1984. Ice nucleus measurement with a continuous flow chamber. Q. J. R. Meteorol. Soc., 110: 75–84.

Knudsen, J.G. and Katz, D.L., 1958. Fluid Dynamics and Heat Transfer. McGraw Hill, New York, N.Y., 576 pp.

Kumai, M., 1982. Formation of ice crystals and dissipation of supercooled fog by artificial nucleation, and variations of crystal habit at early growth stages. J. Appl. Meteorol., 21: 579–587.

Langer, G., 1973. Evaluation of NCAR ice nucleus counter, Part I. Basic operation. J. Appl. Meteorol., 12: 1000–1011.

Mossop, S.C., 1985. The origin and concentration of ice crystals in clouds. Bull. Am. Meteorol. Soc., 66: 264–273.

Mozurkewich, M., 1986. Aerosol growth and the condensation coefficient for water: a review. Aerosol Sci. Technol., 5: 223–236.

Nimitz, K.S. and Plooster, M., 1980. Atmospheric Cloud Physics Laboratory (ACPL) Simulation System Mathematical Description. General Electric Co., Huntsville Operations, Huntsville, Ala., 89 pp.

Plooster, M.N., 1985. Computer Models for Simulation of Experiments in the Atmospheric Cloud Physics Laboratory (ACPL). Report 5-31701, Denver Research Institute, Univ. Denver, Denver, Colo., 78 pp.

Pruppacher, H.R. and Klett, J.D., 1978. Microphysics of Clouds and Precipitation. D. Reidel, Boston, 714 pp.

Ranz, W.E. and Wong, J.B., 1952. Impaction of dust and smoke particles on surface and body collectors. Ind. Eng. Chem., 44: 1372–1381.

Saxena, V.K., Buford, J.N. and Kassner, H.L., Jr., 1970. Operation of a thermal diffusion chamber for measurements on cloud condensation nuclei. J. Atmos. Sci., 27: 73–80.

Saxena, V.K. and Carstens, J.C., 1971. On the operation of cylindrical thermal diffusion cloud chambers. J. Rech. Atmos., 5: 11–23.

Sinnarwalla, A.M. and Alofs, D.J., 1973. A cloud nucleus counter with long available growth time. J. Appl. Meteorol., 12: 831–835.

Tomlinson, E.M., 1980. A New Horizontal Gradient, Continuous Flow, Ice Thermal Diffusion Chamber and Detailed Observation of Condensation-Freezing and Deposition Nucleation. Ph.D. Dissertation, Department of Meteorology, University of Utah, 108 pp.

Tomlinson, E.M. and Fukuta, N., 1985. A new horizontal gradient, continuous flow, ice thermal diffusion chamber. J. Atmos. Oceanic Technol., 2: 448–467.

Twomey, S., 1972. Measurements of the size of natural cloud nuclei by means of Nuclepore filters. J. Atmos. Sci., 29: 318–321.

Vali, G., 1985. Nucleation terminology. J. Aerosol Sci., 16: 575–576.

Vali, G., Rogers, D., Gordon, G., Saunders, C.P.R., Reischel, M. and Black, R., 1978. Aerosol and Nucleation Research in Support of NASA Cloud Physics Experiments in Space. Final Report, Department of Atmospheric Science, University of Wyoming, Laramie, Wyo., 86 pp.

Zamurs, J., Lala, G. and Jiusto, J.E., 1977. Factors affecting ice nucleus concentration measurements with a static vapor-diffusion chamber. J. Appl. Meteorol., 16: 419–421.